Fluidization behavior of stirred gas–solid fluidized beds

A combined X-ray and CFD–DEM–IBM study

van der Sande, P.C.; de Munck, M.J.A.; Wu, K.; Rieder, D.R.; van den Eertwegh, D.E.A.; Wagner, E.C.; Meesters, G.M.H.; Peters, E.A.J.F.; Kuipers, J.A.M.; van Ommen, J.R.

DOI
10.1016/j.cej.2024.155944

Publication date
2024

Document Version
Final published version

Published in
Chemical Engineering Journal

Chemical Engineering Journal 499 (2024) 155944

Contents lists available at ScienceDirect

Chemical Engineering Journal

journal homepage: www.elsevier.com/locate/cej

Fluidization behavior of stirred gas–solid fluidized beds: A combined X-ray and CFD–DEM–IBM study

P.C. van der Sande [a,1], M.J.A. de Munck [b,1], K. Wu [a], D.R. Rieder [b], D.E.A. van den Eertwegh [b], E.C. Wagner [a], G.M.H. Meesters [a], E.A.J.F. Peters [b], J.A.M. Kuipers [b], J.R. van Ommen [a,*]

[a] *Product and Process Engineering Group, Department of Chemical Engineering, Delft University of Technology, Van der Maasweg 9, 2629 HZ Delft, The Netherlands*

[b] *Multiphase Reactors Group, Department of Chemical Engineering and Chemistry, Eindhoven University of Technology, P.O. Box 513, 5600 MB Eindhoven, The Netherlands*

ARTICLE INFO

Keywords:
Fluidized bed
Agitation
CFD–DEM–IBM
X-ray imaging
VSBR
Validation

ABSTRACT

Stirred gas–solid fluidized bed reactors are commercially employed in polyolefin manufacturing, but the complex gas–solid contacting dynamics pose challenges in design, scale-up, and operation. In this study, the influence of agitation on the fluidization performance of Geldart B particles was investigated experimentally by X-ray imaging and pressure drop measurements and numerically by Computational Fluid Dynamics (CFD) - Discrete Element Method (DEM) - Immersed Boundary Method (IBM). The experimentally obtained minimum fluidization curve and time-averaged pressure drop show good qualitative agreement with the simulation results. Visual observations underscore that an increase in the angular velocity of the agitator results in reduced bubble size and improved bed homogeneity, as further evidenced by reduced pressure fluctuations. Furthermore, the simulations reveal that while the impeller enhances solids agitation, a proper design study is imperative, considering that static immersed bodies, such as the stirrer shaft, can adversely impact solids motion.

1. Introduction

Gas–solid fluidized beds, in which a gas is passed upward through a bed of settled particles to suspend the particles in a fluid-like state, find widespread applications across various industries requiring good solids mixing, as well as efficient heat and mass transfer [1]. However, for many practical applications, the design, scale-up, and operation of gas–solid fluidized beds remain challenging due to the inherently complex and scale-dependent hydrodynamics. Over time, several methods have been suggested to enhance the performance of fluidized beds by introducing an additional source of energy to the bed, such as gas pulsation, sound, vibration, or agitation [2].

Stirred gas–solid fluidized bed reactors, also referred to as vertical stirred bed reactors (VSBRs), utilize mechanical agitation to introduce external energy into the system. Agitation facilitates improved solids mixing, a high degree of bed homogeneity, improved heat transfer, intensive gas–solid contact, and allows fluidization of cohesive materials [3,4]. Due to these advantageous characteristics, stirred gas–solid fluidized beds are widely applied in industrial processes. One of their most significant applications is in solid-catalyzed gas-phase polymerization [5]. BASF pioneered stirred gas–solid fluidized bed polymerization processes with the introduction of the Novolen vertical stirred bed process for the manufacture of polypropylene in 1969 [6,7]. In this reactor, the gas phase monomer undergoes polymerization with a co-monomer and hydrogen under the influence of a solid catalyst. Effective heat management in these exothermic polymerization reactions is crucial to prevent runaway process conditions that could lead to polymer melting. Heat management is intricately linked to gas–solid contact, but the complex gas–solid contacting principles in these reactors present challenges in design, scale-up, and operation and, therefore, require detailed investigation.

Early studies, such as those by Reed, III and Fenske [3], conducted in the 1950s, explored the effects of agitation in gas–solid fluidized beds. Through pressure drop measurements, they showed that immersed oscillating stirring elements can improve the fluidization quality and increase heat transfer between air and the extended surface in a rectangular vessel. Leva [8] correlated the pressure drop and power requirements in gas–solid fluidized beds agitated by a blade-type agitator. Moreover, Sahoo [4] experimentally investigated the bed expansion and fluctuation in a cylindrical gas–solid fluidized bed with stirred promoters. It was reported that the agitation promotes the

* Corresponding author.
E-mail addresses: P.C.vandersande@tudelft.nl (P.C. van der Sande), J.R.vanOmmen@tudelft.nl (J.R. van Ommen).
[1] These two authors contributed equally to this work.

https://doi.org/10.1016/j.cej.2024.155944
Received 2 July 2024; Received in revised form 2 September 2024; Accepted 16 September 2024
Available online 21 September 2024

Nomenclature

Roman letters

$d_{p,i}$	Particle diameter (m)
e_n	Normal restitution coefficient (–)
e_t	Tangential restitution coefficient (–)
$\mathbf{F}_{contact,i}$	Particle contact force (N)
$\mathbf{g}$	Gravitational acceleration ($m\,s^{-2}$)
I	X-ray intensity on the detector (–)
$\mathbf{I}$	Unit tensor (–)
I_0	X-ray intensity from the source (–)
I_i	Moment of inertia ($kg\,m^2$)
I_{empty}	X-ray intensity of empty reference (–)
I_{full}	X-ray intensity of full reference (–)
k_n	Normal stiffness ($N\,m^{-1}$)
k_t	Tangential stiffness ($N\,m^{-1}$)
m_i	Particle mass (kg)
p_g	Gas pressure (Pa)
Re	Reynolds number (–)
$\mathbf{S}$	Momentum source term ($kg\,m^{-2}\,s^{-2}$)
t	Time (s)
$\mathbf{T}$	Particle torque ($kg\,m\,s^{-2}$)
$\mathbf{u}_g$	Gas velocity ($m\,s^{-1}$)
$\mathbf{r}_i$	Particle position (m)
$\mathbf{v}_i$	Particle velocity ($m\,s^{-1}$)
V_i	Particle volume (m^3)

Greek letters

β	Interface momentum exchange coefficient (–)
$\boldsymbol{\tau}_g$	Stress tensor ($N\,m^{-2}$)
δ_n	Normal overlap (m)
δ_t	Tangential overlap (m)
ϵ_g	Gas holdup (–)
η_n	Normal damping coefficient ($N\,s\,m^{-1}$)
η_t	Tangential damping coefficient ($N\,s\,m^{-1}$)
μ	Attenuation coefficient (–)
μ_g	Gas dynamic viscosity ($kg\,m^{-1}\,s^{-1}$)
ω	Angular velocity ($rad\,s^{-1}$)
ϕ	Solids mass flux ($kg\,m^{-2}\,s^{-1}$)
ρ	Density ($kg\,m^{-3}$)

Sub/superscripts

g	Gas property
i	Individual particle
p	Particle property

Abbreviations

CFD	Computational Fluid Dynamics
DEM	Discrete Element Method
IBM	Immersed Boundary Method
TFM	Two-Fluid Model
VSBR	Vertical Stirred Bed Reactor

fluidization quality by improving particle mixing. Furthermore, Han et al. [9] studied the influence of agitation of a frame impeller on the fluidization performance of Geldart type D particles through experimentation and numerical simulation. They found that agitation facilitates homogeneous fluidization with increased uniformity of particle velocities. More recently, Wang et al. [10] performed a numerical simulation of the fluidization behavior of cohesive powders in stirred gas–solid fluidized beds with a frame impeller. Employing a Two-Fluid Model (TFM), they found that increasing the strength of the mechanical agitation intensifies the movements of the particles, especially in the lateral direction.

Sophisticated computer models, such as Computational Fluid Dynamics (CFD) - Discrete Element Method (DEM), offer a means to gain fundamental insights into the hydrodynamics of stirred gas–solid fluidized beds. It is commonly accepted in the scientific community that CFD–DEM simulations are more accurate, allow more detailed analysis, and have, among others, advantages with respect to polydispersity and non-spherical particles compared to TFM simulations, which tend to be faster and less computationally expensive [11–13]. With the current increase in computational power, CFD–DEM simulations of complex gas–solid systems are becoming more feasible. However, such simulations are very CPU demanding, and therefore, several approaches, such as coarse-graining or application of recurrence CFD (r-CFD), have been developed [14–16].

In this study, we extend a CFD–DEM model with an Immersed Boundary Method (IBM) in order to conduct a fundamental investigation into the fluidization behavior of Geldart B particles in a non-reactive stirred gas–solid fluidized bed reactor. A crucial aspect of using computer models is model verification to ensure its accuracy. To experimentally verify the CFD–DEM–IBM model, a laboratory-scale experimental and a one-on-one computational stirred gas–solid fluidized bed reactor have been developed. This paper focuses on the thorough comparison of the simulations with detailed hydrodynamic features obtained through experimental investigation. Since gas–solid fluidized beds are opaque to visible light, we employed X-ray imaging to visualize the fluidization behavior of the experimental stirred gas–solid fluidized bed. This paper first describes the experimental and simulation methods. Then, the experimental conditions and simulation parameters employed in the study are elaborated on. Subsequently, the results are presented and discussed. Finally, the results are summarized, and conclusions are drawn.

2. Methods and materials

2.1. Experimental methods

2.1.1. Stirred gas–solid fluidized bed setup

The experimental stirred gas–solid fluidized bed reactor consists of a fluidized bed column and an agitating system, as illustrated in Fig. 1(a). The fluidized bed column is comprised of a 90 mm inner-diameter perspex cylinder with a length of 700 mm fitted with a 3 mm thick sintered stainless steel distributor plate. The agitating system comprises a 800 mm long stainless steel shaft with a three-blade PLA rectangular impeller at the bottom, positioned at the height of 50 mm above the distributor plate. The stirrer is mechanically agitated by a motor positioned atop the column. The column contains pressure ports through which the pressure can be measured at a height of 6 mm and 65 mm above the distributor plate.

2.1.2. X-ray imaging

The hydrodynamics of the stirred gas–solid fluidized bed were experimentally assessed using an in-house fast X-ray imaging setup, as depicted in Fig. 1(b). X-ray imaging is a non-invasive imaging technique that can be used to visualize the hydrodynamics of opaque multiphase flows effectively [17,18]. Through X-ray imaging, a 2D projection of the spatial gas–solids distribution in the stirred gas–solid fluidized bed reactor was captured.

The X-ray setup consists of a standard medical-use X-ray source (Yxlon International GmbH) with a maximum energy of 150 keV working in cone beam mode and a 2D detector (Teledyne Dalsa Xineos)

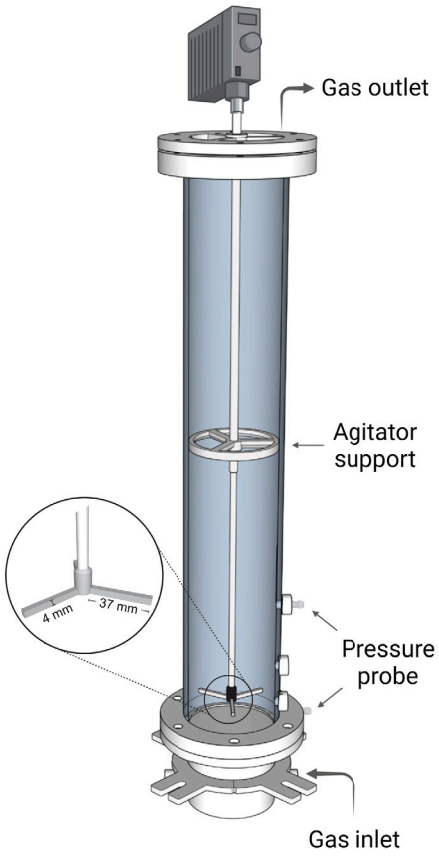

(a) Schematic of the stirred gas-solid fluidized bed reactor, which consists of a fluidized bed column and an agitating system.

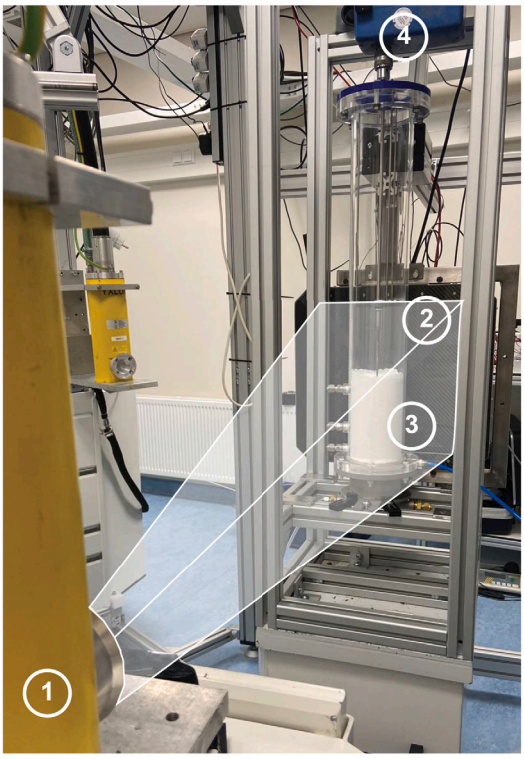

(b) Optical camera photo of the stirred gas-solid fluidized bed reactor comprising the particle bed (3) positioned in between the X-ray source (1) and the X-ray detector (2), with a schematic representation of the X-ray beam. The motor (4) used to agitate the stirrer is positioned atop the column.

Fig. 1. Experimental setup used in this study.

with a theoretical spatial resolution of 0.20 mm placed opposite of the source. X-ray images were acquired at a sampling rate of 50 Hz over a measurement period of 60 s, equating to the acquisition of 3000 images per experiment. The obtained data were then stored for subsequent digital image analysis.

The X-ray measurement principle relies on the attenuation of X-rays traveling in a straight line from an X-ray source to a detector while passing through the material. The transmission of a monochromatic beam of high-energy photons with initial intensity I_0 through a material of constant density is described by the Lambert–Beer law:

$$I(x) = I_0 \exp(-\mu x) \tag{1}$$

Here, $I(x)$ denotes the intensity measured at the detector, μ is the attenuation coefficient, and x is the thickness of the X-ray attenuating material between the source and the detector. For varying attenuation, the measured intensity is the integral effect of local attenuation with the local attenuation coefficient.

Each acquired image is a time-resolved projected 2D intensity map of the stirred gas–solid fluidized bed reactor. A calibration protocol was executed to convert the measurement intensity into a gas holdup. Initially, a reference image of the empty column was captured without the agitating system. Subsequently, the column was filled with the bed material, and a full reference image was obtained. By applying the Lambert–Beer law, the measurement gas holdup map was derived from the measurement intensity map using the empty and full reference, as depicted in Fig. 2. The normalized gas holdup ϵ_g was calculated as follows:

$$\epsilon_g = \frac{\ln(I_{\text{measurement}}/I_{\text{full}})}{\ln(I_{\text{empty}}/I_{\text{full}})} \tag{2}$$

The calibration protocol is discussed in more detail and validated in the work by Wu et al. [19]. It is important to note that the normalized gas holdup in this study ranges from 0.37 to 1, where 1 represents pure gas and 0.37 close packing of solids. Warm colors in the gas holdup map correspond to low X-ray attenuation, indicating high gas concentrations. In contrast, cold colors represent high X-ray attenuation, indicating low gas concentrations.

2.1.3. Pressure measurements

To experimentally determine the minimum fluidization velocity and quantitatively evaluate the quality of fluidization during the measurements, the pressure drop was measured over the powder bed. The gas pressure was probed with a sampling frequency of 1000 Hz using OMEGA PX409-10WG5V pressure transducer positioned at heights of 6 mm and 65 mm above the distributor plate.

The time-averaged pressure drop and standard deviation of the pressure drop are common indicators for assessing fluidization quality. The acquired pressure data was multiplied with the column's cross-sectional area (A) and divided by the mass of the solids (m) and the gravitational acceleration (g) to give the normalized pressure drop ($\Delta PA/(mg)$).

2.2. Simulations

In this work, the CFD–DEM–IBM combination of the CFD framework FoxBerry [20] and the DEM code MercuryDPM [21] is used. The code has been utilized and validated in previous works [13,22]. The gas

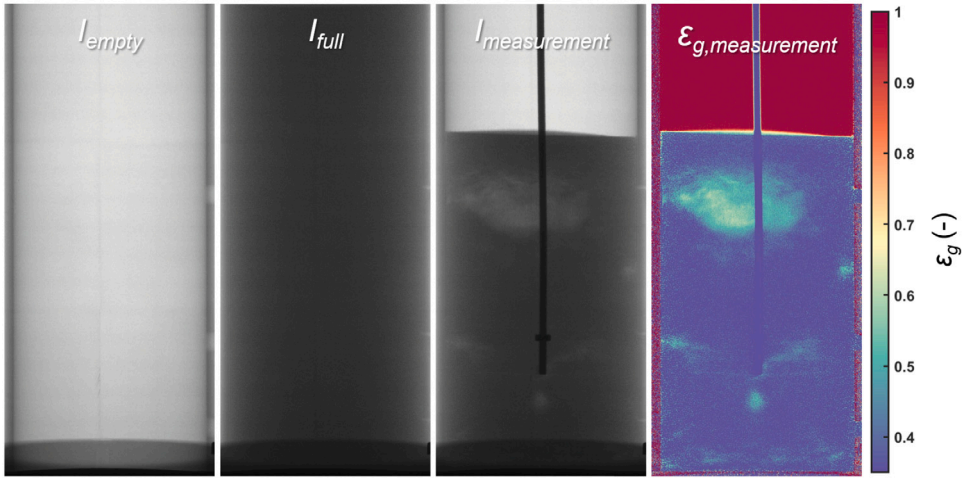

Fig. 2. The measurement gas holdup (ϵ_g) map is computed from the measurement intensity map by employing Lambert–Beer law with an empty and full reference.

phase is described by the continuity equation and the volume-averaged Navier–Stokes equations, respectively given by:

$$\frac{\partial(\epsilon_g \rho_g)}{\partial t} + \nabla \cdot \left(\epsilon_g \rho_g \mathbf{u}_g\right) = 0 \tag{3}$$

$$\frac{\partial \left(\epsilon_g \rho_g \mathbf{u}_g\right)}{\partial t} + \nabla \cdot \left(\epsilon_g \rho_g \mathbf{u}_g \mathbf{u}_g\right) = -\epsilon_g \nabla p_g - \nabla \cdot \left(\epsilon_g \boldsymbol{\tau}_g\right) - \mathbf{S} + \epsilon_g \rho_g \mathbf{g} \tag{4}$$

$\boldsymbol{\tau}_g$ is the gas phase stress tensor using the general Newtonian form. $\mathbf{S}$ represents the momentum source term for the gas–solids interaction, given by:

$$\mathbf{S} = \sum_i 3\pi \mu_g \epsilon_g d_{p,i} \beta \left(\mathbf{u}_g - \mathbf{v}_i\right) D\left(\mathbf{r} - \mathbf{r}_i\right) \tag{5}$$

The momentum source term uses the polynomial distribution function of Deen et al. [23] using a mapping width of $3d_p$. The drag correlation of Beetstra et al. [24] is employed:

$$\beta = 10\frac{(1-\epsilon_g)}{\epsilon_g^2} + \epsilon_g^2\left(1 + 1.5\sqrt{1-\epsilon_g}\right) + \frac{0.413 Re_p}{24\epsilon_g^2}\frac{\left[\epsilon_g^{-1} + 3\epsilon_g(1-\epsilon_g) + 8.4 Re_p^{-0.343}\right]}{\left[1 + 10^{3(1-\epsilon_g)} Re_p^{-0.5-2(1-\epsilon_g)}\right]} \tag{6}$$

Where the Reynolds number is computed via:

$$Re_p = \frac{\epsilon_g \rho_g \left|\mathbf{u}_g - \mathbf{v}_p\right| d_p}{\mu_g} \tag{7}$$

The translational and rotational movement of each individual particle is calculated by solving Newton's equations:

$$m_i \frac{d\mathbf{v}_i}{dt} = -V_i \nabla p_g + 3\pi \mu_g \epsilon_g d_{p,i} \beta \left(\mathbf{u}_g - \mathbf{v}_i\right) + m_i \mathbf{g} + \sum \mathbf{F}_{contact,i} \tag{8}$$

$$I_i \frac{\boldsymbol{\omega}_i}{dt} = \mathbf{T}_i \tag{9}$$

where $\mathbf{v}_i$ is the particle velocity. The forces on the right-hand side for the translational motion (Eq. (8)) are respectively due to the far-field pressure gradient, drag, gravity, and contact forces due to particle–particle or particle–wall collisions. The contact forces are captured by a soft-sphere model originally developed by Cundall and Strack [25]. $\mathbf{T}_i$ is the torque which changes due to the tangential component of the individual contact forces resulting from the linear-spring dashpot model, I_i the moment of inertia and $\boldsymbol{\omega}_i$ the rotational velocity (1/s).

2.2.1. Stirrer and cylinder geometry

Neither the geometry of the column wall nor of the stirrer aligns with the underlying 3D Cartesian grid of the continuous phase. To represent both, a second-order implicit ghost cell Immersed Boundary Method (IBM) is employed [26]. In this method, the coefficients of the discretized momentum equations of the continuous fluid are adapted if the surface of an object intersects with the discretization stencil. This manipulation utilizes a directional, second-order extrapolation to compute the velocity in the immersed cell under the assumption of a no-slip boundary condition at the object's surface. Additionally, if a cell center is located inside the object, the local velocity corresponding to the solid body motion of the object is imposed on the solution.

The cylinder geometry is approximated by a tube with radius R. All required values for the application of the IBM, such as intersection points of grid lines with the cylinder, are determined analytically [27]. In contrast, a mesh in the Standard Tesselation Language format is employed for the complex geometry of the stirrer. There, the surface of the object is approximated by a set of interconnected triangles. To determine the required intersections to apply the IBM, the triangles are first associated with the intersecting Cartesian cells via a triangle/axis-aligned-bounding-box intersection algorithm, and subsequently, ray/triangle intersection calculations are carried out to determine the relevant intersect [28]. The required information is recomputed for each fluid time step, following the rotation of the stirrer mesh. The particle contact with the stirrer and cylinder is covered in the DEM code MercuryDPM as reported by Weinhart et al. [21].

3. Setup

3.1. Experiments

Commercially available Geldart B-type high-purity alumina powder (SASOL) is used as bed material in this study. The powder has a Sauter mean particle diameter of 0.94 mm and a particle density of 1300 kg m^{-3}. For the fluidization experiments, the column was loaded with 774 g of material, constituting a settled bed height of approximately 150 mm. Through pressure drop measurements, of which the results are presented in Section 4.1, the minimum fluidization velocity was experimentally determined to be 32.5 cm s^{-1}.

Throughout all experiments, the inlet gas velocity was controlled at 39.3 cm s^{-1}, corresponding to $1.2u_{mf}$. The influence of agitation on the hydrodynamics was systematically assessed by evaluating the hydrodynamics of a bed without an agitator, a bed with a static agitator, and a bed with an agitator while stirring at angular velocities of 7.2, 10.2, and 13.5 rad s^{-1}. An overview of the experimental parameters is provided in Table 1.

Table 1
Experimental parameters used in this study.

Parameter	Symbol	Value	Unit
Particle diameter	d_p	$9.4{\cdot}10^{-4}$	m
Particle density	ρ_p	1300	kg m^{-3}
Inlet velocity air	u_o	0.393	m s^{-1}
Angular velocity stirrer	ω	7.2 - 10.2 - 13.5	rad s^{-1}
Sampling frequency X-ray	f_{xray}	50	Hz
Measurement run time	t_{meas}	60	s

Table 2
Simulation parameters used in this study.

Parameter	Symbol	Value	Unit
Number of particles	N_p	1 369 215	–
Particle diameter	d_p	$9.4{\cdot}10^{-4}$	m
Particle density	ρ_p	1300	kg m^{-3}
Inlet velocity air	u_0	0.393	m s^{-1}
Angular velocity stirrer	ω	7.2 - 10.2 - 13.5	rad s^{-1}
Friction coefficient	μ_0	0.1	–
Normal coefficient of restitution	e_n	0.74	–
Tangential coefficient of restitution	e_t	0.1	–
Normal stiffness	k_n	3000	N m^{-1}
Tangential stiffness	k_t	1305.6	N m^{-1}
Normal dampening coefficient	η_n	0.0056	N s m^{-1}
Tangential dampening coefficient	η_t	0.012	N s m^{-1}
CFD time step	t_{flow}	$2.5{\cdot}10^{-5}$	s
DEM time step	t_{DEM}	$2.5{\cdot}10^{-6}$	s
Time simulated	t	11	s
Number of grid cells (width)	N_x	100	–
Number of grid cells (depth)	N_y	100	–
Number of grid cells (height)	N_z	400	–

3.2. Simulations

The CFD–DEM-IBM simulations were carried out using a 3D rectangular column with dimensions 0.1×0.1×0.4 m (width ×depth × height) wherein the cylindrical tube with 90 mm inner-diameter is positioned. The main simulation parameters are listed in Table 2. The DEM collision parameters for γ-Al_2O_3 are previously reported by Sutkar et al. [29]. In order to improve the gas phase resolution and the corresponding IBM method, the grid size is chosen to be smaller than the particle diameter. This is allowed by making use of the continuous two-way smoothing function of Deen et al. [23] for the Lagrangian–Eulerian mapping as studied by de Munck et al. [13]. This smoothing function is also subsequently used and validated in previous works, see de Munck et al. [22,30,31]. The boundary conditions for the continuous phase were set as a uniform superficial air velocity equal to 39.3 cm s^{-1} at the bottom and a fixed pressure boundary condition of 1 atm at the top of the domain.

4. Results and discussion

4.1. Minimum fluidization curve

The pressure drop as a function of the superficial gas velocity was acquired through experimentation and simulation using a column without an agitator. It is important to establish that the model can accurately capture the fluidization behavior of the granular bed and thus gives a correct representation of pressure drop. Fig. 3 presents the time-averaged normalized pressure drop ($\Delta PA/(mg)$) as a function of the superficial gas velocity.

At gas velocities below 30 cm s^{-1}, a difference between the simulated and the experimentally obtained time-averaged normalized pressure drop can be observed. Although both curves show a characteristic linear increase in the pressure drop in a fixed bed regime, the simulated pressure drop is slightly higher than the experimentally obtained one. Moreover, by closely evaluating the points at which the plateaus are reached, the minimum fluidization velocity for the alumina powder is found to be approximately 27.5 cm s^{-1} in the simulation and 32.5 cm s^{-1} in the experiment.

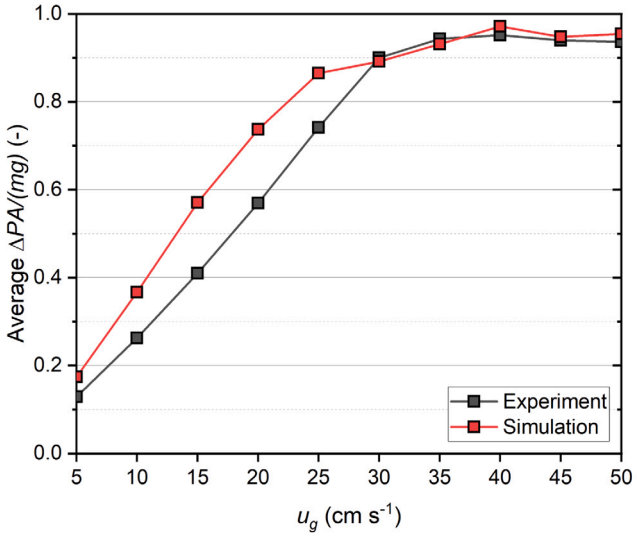

Fig. 3. The time-averaged normalized pressure drop measured at the height of 6 mm above the distributor plate as a function of the superficial gas velocity, u_g.

Two root causes are discerned for these differences. First, the superficial gas velocity is step-wise increased in the simulation, whereafter, the pressure drop data is averaged over a 0.5 s time period. A 0.5 s time period could be insufficient to give a stable averaging pressure, but longer simulation times are very computationally expensive, and therefore a compromise has to be found. In contrast, in the experiment, averaging was performed for a 30 s period after stabilizing the system.

Second, the measured pressure drop in a fixed bed regime is highly susceptible to the packing of solids and meso-structure of the bed. Manual filling in the experimental procedure could give rise to a heterogeneous solids packing, which in turn results in a lower pressure drop as the gas finds a path with lower resistance. Moreover, in the simulation, the meso-structure is less resolved, which increases the tendency of the gas to form bubbles. At higher gas velocities (from 30 cm s^{-1} onward), there is a good agreement between the simulated and the experimentally obtained time-averaged normalized pressure drop, as both curves approach a plateau at an average normalized pressure drop of approximately 0.95 when fluidization is attained. This is in agreement with the theory that pressure drop differences due to different packing vanish, which increases the likelihood that the differences in observed pressure drop are caused by the heterogeneous solids packing in the experiment and the challenges in resolving the meso-structure of the bed in the simulation. Notably, at gas velocities higher than the minimum fluidization velocity, a good agreement is observed, demonstrating that the model can accurately describe the pressure drop over the bed under fluidized conditions, which is key to this work.

4.2. Visualization of the fluidization behavior

A significant advantage of time-resolved X-ray imaging is that it can provide a direct projection of the gas holdup over time, which allows visualization of the fluidization behavior. Similarly, a 2D projection presenting the gas holdup over time can be obtained from the CFD–DEM–IBM simulations. Through displaying representative snapshots, Fig. 4 presents a qualitative comparison of the experimentally observed fluidization behavior and the simulated fluidization behavior for various stirrer settings.

From the experiment-simulation comparison, it becomes evident that the upper part of the bed in the simulations displays more disorderly behavior, especially visible in the splash zone, caused by the formation of larger bubbles. In contrast, the experimental bed shows less frequent and smaller bubbles, thereby displaying less disorderly behavior. The difference could be attributed to differences in the meso-structure of the bed and a slightly different fluidization regime, which can be better understood by the presented data on the minimum fluidization velocity determination.

Here, a discrepancy in the obtained pressure drop at low gas velocities was attributed to a difference in minimum fluidization velocity and the meso-structure of the beds. The same can contribute to the observed difference in fluidization behavior. At, or close to, the point of minimum fluidization, the bed is in a loosely packed state, which allows gas to flow through the meso-structure of the bed. In the experiment, this results in the gas flowing well-distributed through the bed. Therefore, the fluidization behavior observed in the experiment is more homogeneous, and a slightly lower gas holdup is obtained in the snapshots.

In the simulation, a lower minimum fluidization velocity was found, which means that the simulations are performed at a higher u_g/u_{mf} ratio when compared to the experiments. To elucidate this effect, the experiments were also performed at a superficial gas velocity of $45\,\mathrm{cm\,s^{-1}}$. The corresponding X-ray images are included in the supplementary information in Fig. S1. It can be observed that at a velocity of $45\,\mathrm{cm\,s^{-1}}$, the bed displays significantly more chaotic behavior compared to the behavior at the velocity of $39.3\,\mathrm{cm\,s^{-1}}$, despite it only being a 15% increase. Interestingly, now the flow pattern shows stronger similarities to the simulation, suggesting that, indeed, the difference in u_g/u_{mf} ratio could play an important role.

In addition, the meso-structure of the bed is less resolved. This difference in behavior is shown by displaying the temporal evolution of the flow pattern over a time window of $0.4\,\mathrm{s}$ for a rotation speed of $10.2\,\mathrm{rad\,s^{-1}}$ (see supplementary information Fig. S2). When comparing the bottom zone of the experimental and simulated flow patterns in supplementary information Fig. S2, it can be observed that both display the presence of horizontal gas structures directly above the distributor plate. These structures rise up before being dispersed into bubbles by the stirrer. As the meso-structure of the bed is less resolved for the simulation, the gas has the tendency to form bubbles more rapidly in the simulations than in the experiments, as observable in the figure. In turn, the coalescence of the bubbles leads to the formation of larger bubbles that contribute to the disorderly splash zone observed in the simulations. On the contrary, in the experiments, a significantly smaller number of bubbles are formed that display more structured behavior.

Moreover, another reason contributing to the more disorderly behavior could be that the simulated beds have more energy dissipation when compared to the experiments, as was also shown by Li and Kuipers [32],Verma et al. [33]. This would require a more detailed investigation of the effect of the collision parameters on the fluidization characteristics, which is outside the scope of the present paper.

4.3. Time-averaged gas holdup

With the time-resolved gas holdup ϵ_g acquired through X-ray imaging and simulation, a time-averaged gas holdup was computed:

$$\overline{\epsilon}_g(x,z) = \frac{1}{N_{\Delta t}} \sum_{t=t_0}^{t_0+\Delta t} \epsilon_g(x,z,t) \tag{10}$$

where x and z represent the horizontal and vertical positions, and $N_{\Delta t}$ represents the number of images between t_0 and $t_0+\Delta t$. From the time-averaged gas holdup, a line-averaged gas holdup is computed alongside the vertical direction to display the gas holdup over the bed height:

$$\overline{\epsilon}_{g,x}(z) = \frac{1}{N} \sum_{x=1}^{N} \overline{\epsilon}_g(x,z) \tag{11}$$

where N is the number of pixels in the horizontal direction at the height z.

Fig. 5 depicts the time-averaged gas holdup profiles obtained through X-ray imaging (Fig. 5(a)) and simulation (Fig. 5(b)). In both cases, a local increase in gas holdup is visible at an axial position of $50\,\mathrm{mm}$. This increase in gas holdup is attributed to the wakes formed behind the impeller blades. In agreement with the time-resolved snapshots of the fluidization behavior (Fig. 4), it is evident that the wakes, and thereby the local time-averaged gas holdup, increases with increasing angular velocity. The good agreement in wake formation between the experiment and simulation demonstrates that the simulation adequately captures the fluid dynamics in the stirring zone.

At higher axial positions, some deviation between the experiment and the simulation can be observed. The simulation displays a steady increase in the average gas holdup for an increase in the axial position, attributed to the coalescence of bubbles, while in the experiments, less frequent and smaller bubbles appear, resulting in a more uniform system with a lower gas holdup. In the simulations, a clear difference in the top and bottom regions is observed, which is attributed to the rapid coalescence of bubbles. The more disorderly behavior observed in the simulation results in a smooth increase in the time-averaged gas holdup in the splash zone, identifiable at heights between 150 and $200\,\mathrm{mm}$. On the contrary, the more homogeneous bed observed in the experimental results in a sharp increase in gas holdup in the splash zone, identifiable at an axial position of $150\,\mathrm{mm}$. Besides, an increase in the wake volume and the homogeneity of the bed, caused by increasing the angular velocity of the stirrer, was not found to have a significant effect on the time-averaged line-averaged gas holdup.

4.4. Pressure analysis

The gas pressure was measured at the height of $6\,\mathrm{mm}$ and $65\,\mathrm{mm}$ above the distributor plate experimentally and through simulation. Fig. 6 presents the time-averaged normalized pressure drop. It can be observed that the experimentally obtained normalized pressure drop is accurately captured by the simulation at both heights for all agitator settings. At a height of $6\,\mathrm{mm}$, a normalized pressure drop of approximately 0.95 is observed, indicative of a high-quality fluidization both in the experiment and simulation.

Fig. 7 presents the standard deviation of the normalized pressure drop. The standard deviation of the pressure drop in a fluidized bed is correlated with the bubbling dynamics caused by the energy dissipation due to particle collisions and fluid–particle/stirrer–particle interactions. Typically, an increase in fluid–particle/stirrer–particle interactions leads to a higher bed homogeneity and thus a lower pressure drop standard deviation [32,33]. Both the experimentally measured and simulated standard deviations of the pressure drop decrease with increasing angular velocity, suggesting greater bed homogeneity. When increasing the angular velocity, the bubble size is reduced, resulting in a more homogeneous fluidized bed due to the stirring motion. This is in close agreement with reported literature (see Section 1) and visual observations of the hydrodynamic behavior, as discussed in the previous section.

By comparing the experiment and the simulation, it can be observed that the standard deviation of the pressure drop in the simulation results is larger. This is attributed to the more disorderly nature of the bed (see Fig. 4), which in turn is caused by a lower minimum fluidization velocity and a less resolved meso-structure in the simulation, which resulted in more rapid bubble formation and coalescence in the simulations compared to the experiments. Yet, both the experiment and simulation clearly depict that the enhanced particle–stirrer interaction by means of mechanical agitation improves bed homogeneity, which is desirable in applications that require excellent gas–solid contacting.

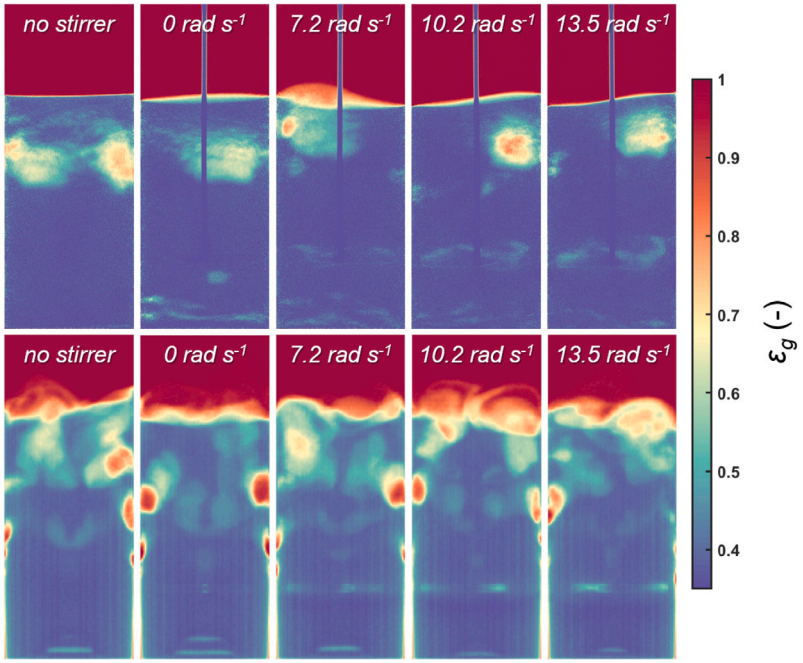

Fig. 4. Typical snapshots of the fluidization behavior at a superficial gas velocity of $39.3\,\mathrm{cm\,s^{-1}}$ for various stirrer settings obtained through experimental X-ray imaging (top) and simulation (bottom).

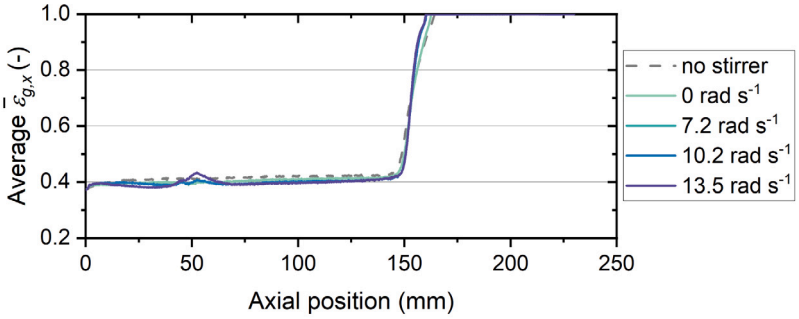

(a) Time-averaged gas holdup over the axial position acquired through X-ray imaging experiments.

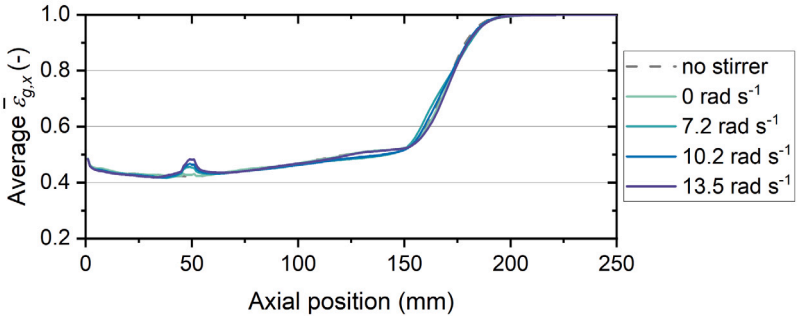

(b) Time-averaged gas holdup over the axial position acquired through simulation.

Fig. 5. Influence of the angular velocity on the time-averaged gas holdup over the axial position.

4.5. Solids mass flux

The CFD–DEM–IBM simulations allow one to study the solids motion and mass flux in more detail, which is not attainable via the currently applied experimental measurements. Experimental techniques such as positron emission particle tracking (PEPT), radioactive particle tracking (RPT), and X-ray particle velocimetry (XPTV) can be used for comparing the solids mass flux obtained from experiments and simulation [34,35], which is not pursued in this work but can serve as an extension of this study. The time-averaged solids mass fluxes for the x- and z-directions are obtained by multiplying the local solids holdup with the obtained average particle velocities of all particles in the cell of interest. This is captured by:

$$\langle \boldsymbol{\phi}_m \rangle = \left\langle \mathbf{v}_p \rho_p \left(1 - \epsilon_g\right) \right\rangle \tag{12}$$

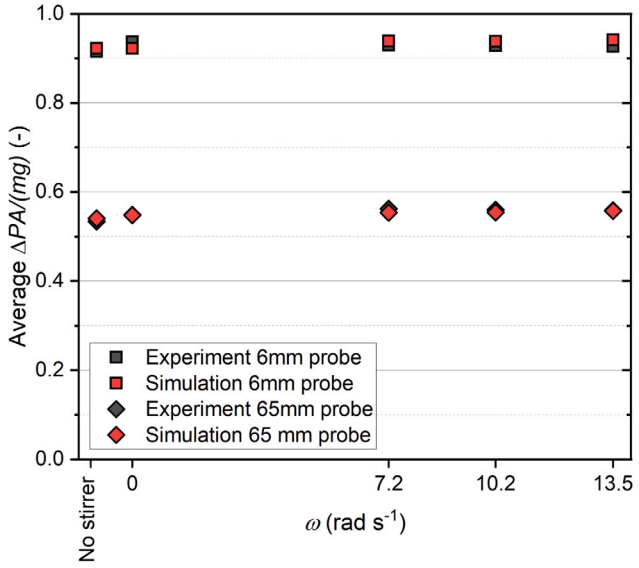

Fig. 6. The influence of agitation on the time-averaged normalized pressure drop.

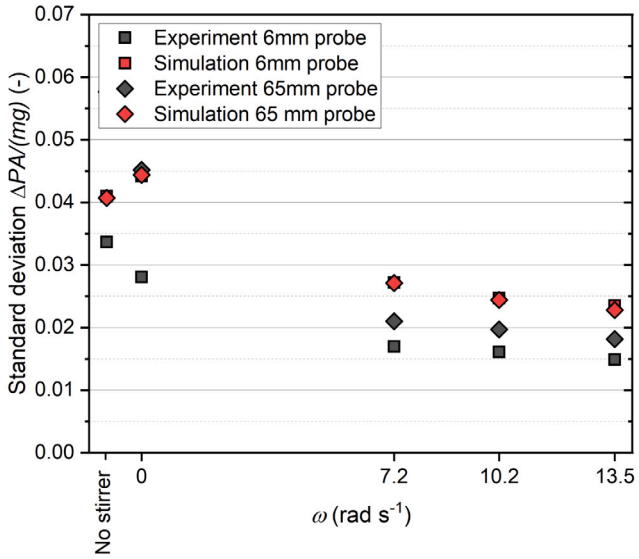

Fig. 7. The influence of agitation on the standard deviation of the pressure drop.

First, the time-averaged solids mass flux for the x-direction is discussed at heights equal to 5, 7.5, 10, and 15 cm. Fig. 8 shows the altered time-averaged x-component of the solids mass flux for the normalized column diameter (x/W) under the influence of agitation. It can be noticed that at a height of 5 cm, where the stirrer is located, the x-component of the solids mass flux is significantly altered due to the rotating stirrer (Fig. 8(a)). Following the stirrer rotation speed, the magnitude of the solids mass flux is increased as the solids are agitated by the stirrer motion. On the contrary, the effect of the stirrer rotational motion is less pronounced at higher axial positions. It can even be concluded that the stirrer shaft acts as a static immersed body, reducing the flowability of the solids material, clearly observed in Figs. 8(b), 8(c) and 8(d) where the case without the stirrer results in a higher x-component of the solids mass flux. Besides, it should be noted that at these heights, the stirrer blades are less influential as they are placed lower inside the bed. Therefore, solids motion is mainly dominated by the gas–solid interaction, as evident from the mass flux in Fig. 8(d) caused by the splash zone.

Fig. 9 represents the solids mass flux z-component at heights equal to 5, 7.5, 10, and 15 cm for the normalized column diameter (x/W). Complementary to the x-component, the stirrer blade rotation alters the solids mass flux directly at the vertical position of the stirrer, as observed in Fig. 9(a). At higher angular velocities, the solids mass flux is increased, especially in the region of 0.25 and 0.75 of the normalized column diameter (x/W). Based on the gas holdup data, this can be better understood by the fact that bubbles are created by the stirrer rotation. The bubble wake provides a transport mechanism for the solids. Subsequently, at h = 7.5 cm (Fig. 9(b)), this rising mechanism results in a symmetrical solids mass flux, which is higher at the sides of the column for the higher stirrer rotations, while being lower in the column center. This pattern is further evolving due to the preferential bubble pathway, resulting in a symmetrical solids mass flux at h = 10 cm and 15 cm. This symmetrical solids mass flux is influenced by the immersed object in the center of the column, which becomes clear by comparing the 0 rad s^{-1} and the case without a stirrer. By a detailed comparison between these cases, it is observed that the immersed static shaft object gives rise to a symmetrical flow pattern, which is not discerned in the case without the stirrer.

Based on the discussions both on the x- and z-components of the solids mass flux, it becomes evident that the solids agitation is improved directly near the stirrer blades, while further up in the bed, the solids agitation is reduced due to the shaft, which acts as a static immersed body. This highlights that assisted fluidization through a vertically placed stirrer can improve the solids agitation. Still, a proper design study needs to be performed as static immersed bodies (e.g. the stirrer shaft) negatively influence the solids motion [19].

5. Conclusions

In this study, the influence of agitation of a vertical three-blade agitator on the fluidization performance of Geldart B particles in a laboratory-scale column is experimentally investigated through X-ray imaging and pressure drop measurements and numerically through CFD–DEM–IBM simulation. The influence of agitation was systematically assessed by evaluating the fluidization behavior of a bed without an agitator, a bed with a static agitator, and a bed with an agitator while stirring at angular velocities of 7.2, 10.2, and 13.5 rad s^{-1}, at $1.2u_{mf}$.

The simulated minimum fluidization curve and time-averaged pressure drop are in qualitative agreement with the experimentally obtained ones, which validates the numerical model. Direct visualization of the fluidization behavior shows that an increase in the angular velocity of the agitator results in reduced bubble size, improved bed homogeneity, and the formation of wakes behind the impeller blades. The reduced bubble size and improved bed homogeneity are further substantiated by the observed decreasing standard deviation of the pressure drop for an increasing angular velocity. Moreover, the agreement between the experiment and simulation in wake formation is good, demonstrating that the simulation adequately captures the fluid dynamics in the stirring zone. Deviations between the simulations and experiments in the gas holdup at the top of the bed were attributed to a slightly lower minimum fluidization velocity and less-resolved mesostructure of the bed in the simulations, which results in more intense bubbling and a more disorderly splash zone. An in-depth analysis of the solids flow field through simulation shows that the solids agitation is improved directly near the stirrer blades, while higher up in the bed, the solids agitation is reduced due to the shaft, which acts as a static immersed body. This emphasizes that while assisted fluidization through a vertically placed stirrer can improve the solids agitation, a proper design study is crucial as static immersed bodies, such as the stirrer shaft, negatively influence the solids motion.

Besides contributing to a further understanding of the hydrodynamics of stirred gas–solid fluidized beds, this work provides a validated

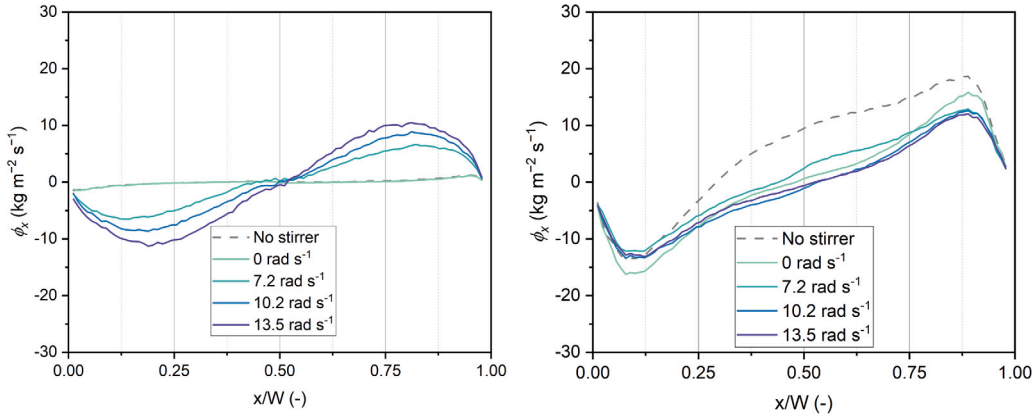

(a) x-component mass flux at a height of 5 cm. (b) x-component mass flux at a height of 7.5 cm.

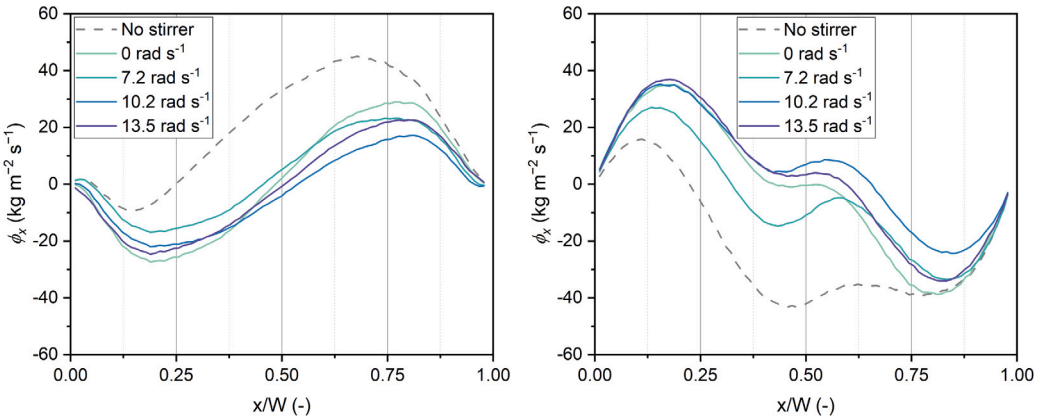

(c) x-component mass flux at a height of 10 cm. (d) x-component mass flux at a height of 15 cm.

Fig. 8. The x-component mass flux at various heights in the bed as for various stirrer settings. Note that the vertical axes have different limits for visibility purposes.

CFD–DEM–IBM simulation method that can be used to simulate fluidized beds with moving internals, such as stirrers. By implementing approaches that speed up the simulation run time, such as coarse-graining and r-CFD, future investigations could aid in optimizing, intensifying, and scaling the systems for industrial applications, such as polyolefin manufacturing.

CRediT authorship contribution statement

P.C. van der Sande: Writing – review & editing, Writing – original draft, Visualization, Validation, Software, Methodology, Investigation, Formal analysis, Data curation, Conceptualization. **M.J.A. de Munck:** Writing – review & editing, Writing – original draft, Visualization, Validation, Software, Methodology, Investigation, Formal analysis, Data curation, Conceptualization. **K. Wu:** Writing – review & editing, Writing – original draft, Software, Formal analysis, Data curation. **D.R. Rieder:** Writing – review & editing, Software, Methodology, Investigation. **D.E.A. van den Eertwegh:** Writing – review & editing, Software, Methodology, Investigation. **E.C. Wagner:** Writing – review & editing, Software, Methodology, Investigation, Data curation. **G.M.H. Meesters:** Writing – review & editing, Supervision, Project administration, Conceptualization. **E.A.J.F. Peters:** Writing – review & editing, Supervision, Project administration, Conceptualization. **J.A.M. Kuipers:** Writing – review & editing, Supervision, Project administration, Funding acquisition, Conceptualization. **J.R. van Ommen:** Writing – review & editing, Supervision, Project administration, Funding acquisition, Conceptualization.

Declaration of competing interest

The authors declare the following financial interests/personal relationships which may be considered as potential competing interests: J.R. van Ommen reports financial support was provided by Dutch Research Council. J.A.M. Kuipers reports financial support was provided by Dutch Research Council. If there are other authors, they declare that they have no known competing financial interests or personal relationships that could have appeared to influence the work reported in this paper.

Data availability

Data will be made available on request.

Acknowledgments

This research received funding from the Dutch Research Council (NWO) in the framework of the ENW PPP Fund for the top sectors and from the Ministry of Economic Affairs in the framework of the “PPS-toeslagregeling”.

The authors also would like to thank SURFsara and NWO domain Science for the use of the Snellius supercomputer facilities.

Appendix A. Supplementary data

Supplementary material related to this article can be found online at https://doi.org/10.1016/j.cej.2024.155944.

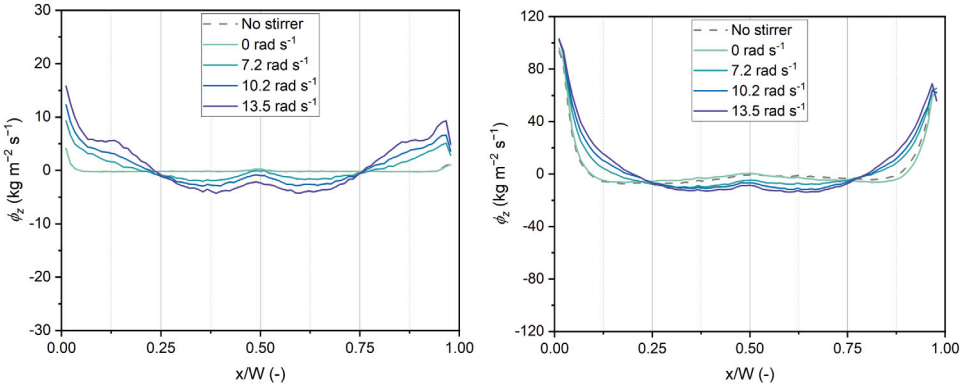

(a) z-component mass flux at a height of 5 cm. (b) z-component mass flux at a height of 7.5 cm.

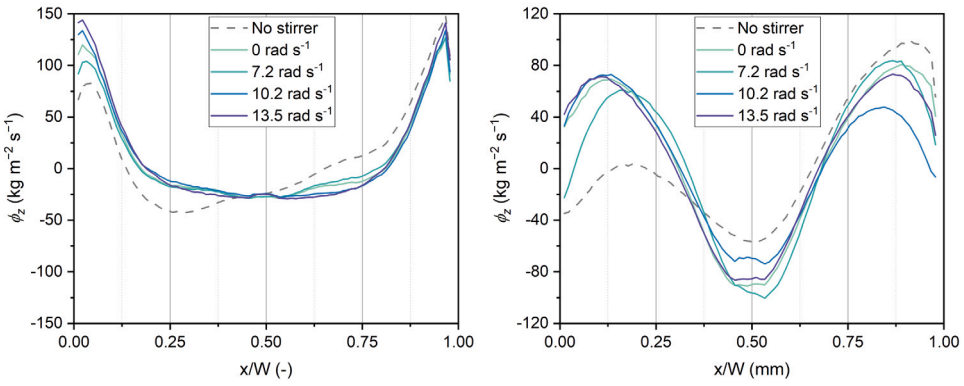

(c) z-component mass flux at a height of 10 cm. (d) z-component mass flux at a height of 15 cm.

Fig. 9. The z-component mass flux at various heights in the bed as for various stirrer settings. Note that the vertical axes have different limits for visibility purposes.

References

[1] L.S. Fan, C. Zhu, Principles of Gas-Solid Flows, Cambridge University Press, Port Chester, NY, United States, 1999.

[2] V. Francia, K. Wu, M.O. Coppens, Dynamically structured fluidization: Oscillating the gas flow and other opportunities to intensify gas-solid fluidized bed operation, Chem. Eng. Process. - Process Intensif. 159 (2021) 108143.

[3] T.M. Reed, III, M.R. Fenske, Effects of agitation on gas fluidization of solids, Ind. Eng. Chem. 47 (2) (1955) 275–282.

[4] A. Sahoo, Bed expansion and fluctuation in cylindrical gas solid fluidized beds with stirred promoters, Adv. Powder Technol. 22 (6) (2011) 753–760.

[5] A.B. Gorbach, S.D. Naik, W.H. Ray, Dynamics and stability analysis of solid catalyzed gas-phase polymerization of olefins in continuous stirred bed reactors, Chem. Eng. Sci. 55 (20) (2000) 4461–4479.

[6] H. Trieschmann, W. Rau, T. Jacobsen, H. Pfannmueller, Polymerization of propylene with ziegler catalysts in a stirred gas phase reactor, (3,652,527) 1972.

[7] W. Rau, H.G. Trieschmann, K. Wisseroth, Methods of removing heat from polymerization reactions of monomers in the gas phase, (4,012,573) 1977.

[8] M. Leva, Pressure drop and power requirements in a stirred fluidized bed, AIChE J. 6 (4) (1960) 688–692.

[9] Y. Han, J.J. Wang, X.P. Gu, L.F. Feng, G.H. Hu, Homogeneous fluidization of geldart D particles in a gas–solid fluidized bed with a frame impeller, Ind. Eng. Chem. Res. 51 (50) (2012) 16482–16487.

[10] S. Wang, Y. Chen, Y. Jia, R. Tian, Q. Sun, J. Fan, Y. Ma, Numerical simulation of flow behavior of particles in a gas-solid stirred fluidized bed, Powder Technol. 338 (2018) 119–128.

[11] M. van Sint Annaland, G. Bokkers, M. Goldschmidt, O. Olaofe, M. van der Hoef, J. Kuipers, Development of a multi-fluid model for poly-disperse dense gas-solid fluidized beds Part I: model derivation and numerical implementation, Chem. Eng. Sci. 64 (20) (2009) 4222–4236.

[12] V. Verma, J.T. Padding, A novel approach to MP-PIC: Continuum particle model for dense particle flows in fluidized beds, Chem. Eng. Sci.: X 6 (2020) 100053.

[13] M.J.A. de Munck, J.B. van Gelder, E.A.J.F. Peters, J.A.M. Kuipers, A detailed gas-solid fluidized bed comparison study on CFD-DEM coarse-graining techniques, Chem. Eng. Sci. 269 (2023) 118441.

[14] M. Sakai, S. Koshizuka, Large-scale discrete element modeling in pneumatic conveying, Chem. Eng. Sci. 64 (3) (2009) 533–539.

[15] T. Lichtenegger, S. Pirker, Recurrence CFD – A novel approach to simulate multiphase flows with strongly separated time scales, Chem. Eng. Sci. 153 (2016) 394–410.

[16] T. Lichtenegger, E. Peters, J. Kuipers, S. Pirker, A recurrence CFD study of heat transfer in a fluidized bed, Chem. Eng. Sci. 172 (2017) 310–322.

[17] K. Wu, E.C. Wagner, O. Ochkin-Koenig, M. Franck, D. Weis, G.M.H. Meesters, J.R. van Ommen, Time-resolved X-ray study of assisted fluidization of cohesive micron powder: On the role of mechanical vibration, Chem. Eng. J. 470 (2023) 143936.

[18] M. Errigo, P. Lettieri, M. Materazzi, X-ray imaging techniques for gas–solid fluidized beds: A technical review, Particuology (2023).

[19] K. Wu, R. Kamphorst, A. Bakker, J. Ford, E.C. Wagner, O. Ochkin-Koenig, M. Franck, D. Weis, G.M. Meesters, J.R. van Ommen, Stirrer design for improving fluidization of cohesive powder: A time-resolved X-ray study, Chem. Eng. Sci. 294 (2024) 120069.

[20] S. Kamath, M.V. Masterov, J.T. Padding, K.A. Buist, M.W. Baltussen, J.A.M. Kuipers, Parallelization of a stochastic Euler-Lagrange model applied to large scale dense bubbly flows, J. Comput. Phys.: X 8 (2020) 100058.

[21] T. Weinhart, L. Orefice, M. Post, M.P. van Schrojenstein Lantman, I.F. Denissen, D.R. Tunuguntla, J.M. Tsang, H. Cheng, M.Y. Shaheen, H. Shi, P. Rapino, E. Grannonio, N. Losacco, J. Barbosa, L. Jing, J.E. Alvarez Naranjo, S. Roy, W.K. den Otter, A.R. Thornton, Fast, flexible particle simulations — An introduction to MercuryDPM, Comput. Phys. Comm. 249 (2020) 107129.

[22] M.J.A. de Munck, E.A.J.F. Peters, J.A.M. Kuipers, Fluidized bed gas-solid heat transfer using a CFD-DEM coarse-graining technique, Chem. Eng. Sci. 280 (2023) 119048.

[23] N.G. Deen, M. van Sint Annaland, J.A.M. Kuipers, Multi-scale modeling of dispersed gas-liquid two-phase flow, Chem. Eng. Sci. 59 (8–9) (2004) 1853–1861.

[24] R. Beetstra, M.A. van der Hoef, J.A.M. Kuipers, Drag Force of Intermediate Reynolds Number Flow Past Mono- and Bidisperse Arrays of Spheres, AIChE J. 53 (2007) 489–501.

[25] P.A. Cundall, O.D.L. Strack, A discrete numerical model for granular assemblies, Geotechnique 29 (1) (1979) 47–65.

[26] N.G. Deen, S.H.L. Kriebitzsch, M.A. van der Hoef, J.A.M. Kuipers, Direct numerical simulation of flow and heat transfer in dense fluid–particle systems, Chem. Eng. Sci. 81 (2012) 329–344.

[27] A. Eghbalmanesh, A. Fathiganjehlou, D.R. Rieder, M. Hoogendoorn, M. Miloshevska, M.W. Baltussen, E.A.J.F. Peters, K.A. Buist, J.A.M. Kuipers, CFD-validated pore network modeling of packed beds of non-spherical particle, Chem. Eng. Sci. 283 (2024) 119396.
[28] T. Akenine-Möller, E. Haines, N. Hoffman, A. Pesce, M. Iwanicki, S. Hillaire, Real-Time Rendering, Fourth Edition, CRC Press, 2018, pp. 1–1178.
[29] V.S. Sutkar, N.G. Deen, B. Mohan, V. Salikov, S. Antonyuk, S. Heinrich, J.A.M. Kuipers, Numerical investigations of a pseudo-2D spout fluidized bed with draft plates using a scaled discrete particle model, Chem. Eng. Sci. 104 (2013) 790–807.
[30] M.J.A. de Munck, E.A.J.F. Peters, J.A.M. Kuipers, CFD-DEM Fluidized Bed Drying Study Using a Coarse-Graining Technique, Ind. Eng. Chem. Res. 62 (48) (2023) 20911–20920.
[31] M.J.A. de Munck, E.A.J.F. Peters, J.A.M. Kuipers, CFD-DEM modeling and validation of solids drying in a gas-fluidized bed, Chem. Eng. Sci. 291 (2024) 119922.
[32] J. Li, J.A.M. Kuipers, Effect of competition between particle-particle and gas-particle interactions on flow patterns in dense gas-fluidized beds, Chem. Eng. Sci. 62 (13) (2007) 3429–3442.
[33] V. Verma, N.G. Deen, J.T. Padding, J.A.M. Kuipers, Two-fluid modeling of three-dimensional cylindrical gas-solid fluidized beds using the kinetic theory of granular flow, Chem. Eng. Sci. 102 (2013) 227–245.
[34] P.C. van der Sande, J. de Mooij, E.C. Wagner, G.M.H. Meesters, J.R. van Ommen, Single-photon emission radioactive particle tracking method for hydrodynamic evaluation of multi-phase flows, Particuology (2024).
[35] M. Errigo, C. Windows-Yule, M. Materazzi, D. Werner, P. Lettieri, Non-invasive and non-intrusive diagnostic techniques for gas-solid fluidized beds – A review, Powder Technol. 431 (2024) 119098.